




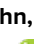











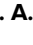







# Three dimensional low-mode areal-density non-uniformities in indirect-drive implosions at the National Ignition Facility

Cite as: Phys. Plasmas **28**, 042708 (2021); <https://doi.org/10.1063/5.0043589>

Submitted: 12 January 2021 . Accepted: 20 March 2021 . Published Online: 15 April 2021

 D. T. Casey,  O. L. Landen,  E. Hartouni,  R. M. Bionta,  K. D. Hahn,  P. L. Volegov,  D. N. Fittinghoff,  V. Geppert-Kleinrath, C. H. Wilde, J. L. Milovich, V. A. Smalyuk, J. E. Field,  O. A. Hurricane,  A. B. Zylstra,  A. L. Kritcher,  D. S. Clark,  C. V. Young,  R. C. Nora,  D. A. Callahan, B. J. MacGowan,  D. H. Munro, B. K. Spears,  J. L. Peterson,  J. A. Gaffney,  K. D. Humbird, M. K. G. Kruse,  A. S. Moore,  D. J. Schlossberg,  M. Gatu-Johnson, and  J. A. Frenje

## COLLECTIONS

Note: This paper is part of the Special Collection: Papers from the 62nd Annual Meeting of the APS Division of Plasma Physics. Note: Paper VII 3, Bull. Am. Phys. Soc. 65 (2020).

 This paper was selected as Featured



View Online



Export Citation



CrossMark



Physics of Plasmas  
Features in Plasma Physics Webinars

Register Today!

# Three dimensional low-mode areal-density non-uniformities in indirect-drive implosions at the National Ignition Facility

Cite as: Phys. Plasmas **28**, 042708 (2021); doi: [10.1063/5.0043589](https://doi.org/10.1063/5.0043589)

Submitted: 12 January 2021 · Accepted: 20 March 2021 ·

Published Online: 15 April 2021












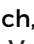




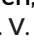
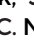









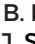



View Online



Export Citation



CrossMark

D. T. Casey,<sup>1,a),b)</sup>  O. L. Landen,<sup>1</sup>  E. Hartouni,<sup>1</sup>  R. M. Bionta,<sup>1</sup>  K. D. Hahn,<sup>1</sup>  P. L. Volegov,<sup>2</sup>   
D. N. Fittinghoff,<sup>1</sup>  V. Geppert-Kleinrath,<sup>2</sup>  C. H. Wilde,<sup>2</sup>  J. L. Milovich,<sup>1</sup>  V. A. Smalyuk,<sup>1</sup>  J. E. Field,<sup>1</sup>  
O. A. Hurricane,<sup>1</sup>  A. B. Zylstra,<sup>1</sup>  A. L. Kritcher,<sup>1</sup>  D. S. Clark,<sup>1</sup>  C. V. Young,<sup>1</sup>  R. C. Nora,<sup>1</sup>   
D. A. Callahan,<sup>1</sup>  B. J. MacGowan,<sup>1</sup>  D. H. Munro,<sup>1</sup>  B. K. Spears,<sup>1</sup>  J. L. Peterson,<sup>1</sup>  J. A. Gaffney,<sup>1</sup>   
K. D. Humbird,<sup>1</sup>  M. K. G. Kruse,<sup>1</sup>  A. S. Moore,<sup>1</sup>  D. J. Schlossberg,<sup>1</sup>  M. Gatu-Johnson,<sup>3</sup>  and J. A. Frenje<sup>3</sup> 

## AFFILIATIONS

<sup>1</sup>Lawrence Livermore National Laboratory, Livermore, California 94550, USA

<sup>2</sup>Los Alamos National Laboratory, Los Alamos, New Mexico 87545, USA

<sup>3</sup>Massachusetts Institute of Technology, Cambridge, Massachusetts 02139, USA

**Note:** This paper is part of the Special Collection: Papers from the 62nd Annual Meeting of the APS Division of Plasma Physics.

**Note:** Paper VII 3, Bull. Am. Phys. Soc. **65** (2020).

<sup>a)</sup>Invited speaker.

<sup>b)</sup>Author to whom correspondence should be addressed: [casey21@llnl.gov](mailto:casey21@llnl.gov)

## ABSTRACT

To achieve hotspot ignition, an inertial confinement fusion implosion must achieve high hotspot pressure that is inertially confined by a dense shell of DT fuel. This requires a symmetric implosion having high in-flight shell velocity and high areal density at stagnation. The size of the driver and scale of the capsule required can be minimized by maintaining a high efficiency of energy coupling from the imploding shell to the hotspot. Significant 3D low mode asymmetries, however, are commonly observed in indirect-drive implosions and reduce the coupling of shell kinetic energy to the hotspot. To better quantify the magnitudes and impacts of shell density asymmetries, we have developed new analysis techniques and analytic models [Hurricane *et al.*, Phys. Plasmas **27**(6), 062704 (2020)]. To build confidence in the underlying data, we have also developed an analytic neutron transport model to cross-compare two independent measurements of asymmetry, which shows excellent agreement across shots for mode-1 ( $\ell = 1$ ). This work also demonstrates that asymmetry can introduce potential sampling bias into down-scattered ratio measurements causing the solid-angle-average and uncertainty-weighted-average down-scattered ratios to differ significantly. Diagnosing asymmetries beyond mode-1 ( $\ell > 1$ ) presents significant challenges. Using new diagnostic instruments and analysis techniques, however, evidence of significant Legendre mode P2 ( $\ell = 2$ ,  $m = 0$ ) and additional 3D asymmetries ( $\ell > 1$ ,  $m \neq 0$ ) are beginning to emerge from the high precision activation diagnostic data (real-time nuclear activation detectors) and down-scattered neutron imaging data.

Published under license by AIP Publishing. <https://doi.org/10.1063/5.0043589>

## I. INTRODUCTION

Inertial confinement fusion (ICF) experiments, like those performed at the National Ignition Facility (NIF),<sup>1</sup> implode capsules of deuterium and tritium fuel to high densities and temperatures to initiate alpha-particle self-heating and fusion burn.<sup>2,3</sup> In indirect drive, a laser irradiates a high-Z cylindrical hohlraum, which produces a nearly uniform, thermal, x-ray drive. This x-ray drive is then used to ablate an outer capsule shell imploding the remaining cryogenically frozen DT shell-mass inward. To achieve ignition, the DT hotspot must have

enough energy density confined for a sufficient time to spark hotspot self-heating and start a burn wave through the dense DT shell. This requirement can also be expressed as a requirement on the product of hotspot pressure  $P$ , a measure of the energy density, and the confinement time of that energy  $\tau$  or  $P\tau$ .<sup>4,5</sup>  $P\tau$  required to achieve ignition derives from a hotspot power balance between the alpha heating power and power losses (such as conduction and radiation) that depends on several factors (including the hotspot temperature, the amount radiative reabsorption, and radiative loss from higher-Z

ablator mix, etc.) but roughly for typical hotspot ignition designs,  $P\tau$  must exceed  $\sim 50$  atm s.<sup>6</sup> To produce high  $P\tau$ , an implosion must have high in-flight implosion velocity ( $v_{imp}$ ), efficient coupling between the inflight shell and hotspot, and high  $\int \rho dr$  or areal-density ( $\rho R$ ) at stagnation.

Three-dimensional (3D)  $\rho R$  asymmetries reduce the coupling of the shell kinetic energy and the confinement of that energy. We can use a simplified two-piston system<sup>7</sup> that was designed to treat Legendre mode-1 ( $\ell = 1$ ) asymmetry (or P1) producing relationships between asymmetry (where  $f$  is a metric for asymmetry) and performance such as the following:  $P\tau$  normalized by the idealized 1D symmetric  $P\tau$  (or  $P\tau_{1D}$ ) becomes  $\frac{P\tau}{P\tau_{1D}} \approx (1 - f^2)$ , the yield ( $Y$ ) normalized by idealized 1D symmetric yield ( $Y_{1D}$ ) becomes  $\frac{Y}{Y_{1D}} \approx (1 - f^2)^{10/3}$ , the residual kinetic energy (RKE) of the shell not converted to hotspot energy becomes  $f^2 \approx RKE$ , and  $f = \frac{\rho R_{max} - \rho R_{min}}{\rho R_{max} + \rho R_{min}} \approx \frac{v_{HS}}{v_{imp}}$ . Here  $\rho R_{max}$  and  $\rho R_{min}$  are the maximum and minimum areal-densities of the dense shell, respectively;  $v_{HS}$  is the bulk velocity of the burning hotspot<sup>8</sup> near peak convergence, and  $v_{imp}$  is the peak implosion velocity. Note that these expressions do not include the effects of alpha heating, which will exacerbate the loss in performance. Additionally, recent experiments have been performed with intentional mode-1 induced drive asymmetries,<sup>9,10</sup> and they show similar trends with this model. It has also been shown using hydrodynamic simulations<sup>11</sup> that higher mode asymmetries damage performance similarly, and work is under way to extend these analytic models  $\ell > 1$ .<sup>12</sup>

This paper will outline some of the evidence that NIF implosions are subjected to significant 3D  $\rho R$  asymmetries with observations of  $\ell = 1$ ,  $\ell = 2$ , and beyond. Section II will discuss in detail some observations of  $\ell = 1$  asymmetry including a cross-comparison and validation of those measurements. Section III will discuss ongoing efforts to understand  $\ell = 2$ , and efforts to validate those measurements, as well as evidence for higher mode asymmetries. Finally, Sec. IV will put this work into context and summarize.

II. OBSERVATIONS OF  $\ell = 1$  ASYMMETRY IN 3D

To better understand the performance of ICF implosion experiments, diagnosing the symmetry of the stagnated fuel is paramount. ICF implosions produce copious numbers of 14 MeV D + T neutrons, and nuclear diagnostic measurements such as the neutron imaging systems (NIS),<sup>13-15</sup> neutron time of flight (nTOF),<sup>16,17</sup> magnetic recoil spectrometry (MRS),<sup>18</sup> and neutron activation detectors (NADs)<sup>19</sup> provide a wealth of information about the neutron emitting hotspot and surrounding cold fuel assembly. Because these measures of asymmetry are based on different principles and different components of the emitted neutron spectrum, a model is required to directly compare them. The neutron transport equation can be used to better understand the principles of neutron interactions in an ICF implosion. Generally, the transport equation is difficult to solve explicitly and so is most commonly solved numerically using Monte Carlo (an example code is MCNP)<sup>20</sup> or inverse Monte Carlo (an example described by Chittenden *et al.*)<sup>21</sup> techniques. Also, recently, Crilly *et al.* have developed a deterministic method of characteristics approach for ICF applications.<sup>22</sup> In the following subsections (Sec. II.A and Sec. II.B), it will be shown that under some simplifying assumptions, rough analytic expressions can be obtained from the transport equation that helps

illustrate how these diagnostics respond to asymmetry and provide models that allow cross-comparison and validation of measurements.

A. Understanding the relationship between  $\rho R$  and activation diagnostics (FNAD/RTNADs)

Nuclear activation detector measurements from the flange nuclear activation detector (FNAD)<sup>19,23</sup> and real-time nuclear activation detector (RTNAD)<sup>24</sup> instrument suites, generically referred to as NAD in this manuscript, provide useful measurements of the implosion  $\rho R$  asymmetry in ICF experiments at the NIF by measuring the relative activation produced by a pulse of 14 MeV neutrons in a suite of Zr detectors.<sup>23</sup> To model these interactions we can use a Neumann series expansion of the integral neutron transport equation.<sup>25</sup> This form is helpful because each higher order term can be thought of as successive generations of neutrons having undergone some series of interactions described with interaction cross sections. Practically for this purpose, the first term of the expansion can be used to approximate the unattenuated 14 MeV neutron flux ( $\varphi_{14}$ ), which is closely related to attenuation measurements like the NAD diagnostics. The second term is related to first order neutron scattering processes such as the ratio of 10-12 MeV neutrons to 13-15 MeV neutrons or down-scattered ratio (DSR) measurements by the nTOF, MRS, and NIS diagnostics, which will be discussed in Sec. II B. This first term of the Neumann series can be written as [see also Fig. 1(a)]

$$\varphi_{14}(\mathbf{r}) = \int d^3r' \frac{e^{-\Sigma_t|\mathbf{r}-\mathbf{r}'|}}{4\pi|\mathbf{r}-\mathbf{r}'|^2} s(\mathbf{r}'). \tag{1}$$

Here,  $\Sigma_t$  is the total macroscopic interaction cross section ( $\Sigma_t = n \sigma_t$ , or inverse of the mean free path) and  $s$  is the volumetric source

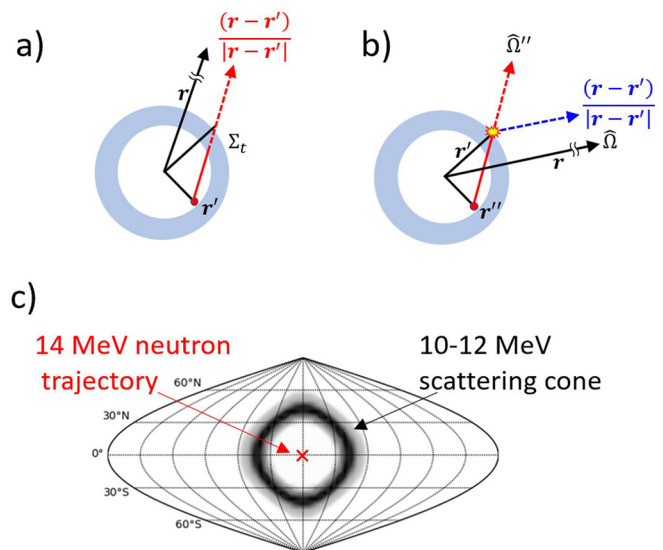


FIG. 1. Schematics of the geometry of Eq. (1) (a) and Eq. (2) (b). (c) Plot of the normalized angular differential scattering cross section  $\sigma_s(\theta)$  probability cast onto a  $\theta/\phi$  sinusoidal projection (“sky”).

distribution. To apply to NAD measurements,  $\Sigma_t$  must describe the interaction probability that a 14 MeV neutron will undergo an interaction that removes it from the Zr activation threshold. NAD measurements are made  $\sim 5$  m away near the NIF chamber wall from the implosion and therefore measurements lend themselves to decomposition into spherical harmonics.<sup>26</sup> Thus, solutions of the 14 MeV neutron flux or time-integrated fluence at the chamber wall are also treated in spherical harmonic decompositions  $\tilde{\varphi}_{14l}^m$  in term of degree ( $l$ ) and order ( $m$ ) of the expansion. Written in terms of spherical harmonics, the resultant unattenuated 14 MeV neutron fluence and the  $\rho R$  appear similar to a convolution by source and scatterer geometric effects. In fact, the addition theorem of spherical harmonics is useful to treat the problem<sup>25</sup> in this way similarly to the convolution theorem of Fourier transforms (Funk Hecke theorem as applied by Basri and Jacobs).<sup>27</sup> Therefore, the 14 MeV yield asymmetry ( $\delta\tilde{Y}_l^m$ ) normalized by the average yield (or  $\delta\tilde{Y}_l^m/Y_{avg}$ ) inferred from the NAD detectors at the chamber wall can be re-expressed as a convolution of  $\rho R$  asymmetry  $\delta\rho R_l^m$  (in  $g/cm^2$ )<sup>28</sup> and a “transport efficiency” term (or  $\tilde{P}$ ) that effectively blurs the details of the  $\rho R$  sky because of source and shell geometry effects

$$\frac{\delta\tilde{Y}_l^m}{Y_{avg}} \sim \left(-0.24 \times \delta\rho R_l^m\right) * \tilde{P}_l^m. \quad (2)$$

Even this simplified form is challenging to solve explicitly, but by making several further simplifying assumptions, we can obtain some useful, if approximate, analytic expressions. First, the form of Eq. (2) has already neglected first order scattering (and so shallow-scattering of neutrons into the threshold of Zr activation is ignored, an effect we can later include with MCNP simulations). Second, realizing that the chamber wall is far away from the source and scatterer, we can make the paraxial approximation (similar to the approach of Volegov *et al.*)<sup>15</sup> so that  $|\mathbf{r} - \mathbf{r}'| \sim R$  and  $\frac{(\mathbf{r}-\mathbf{r}')}{|\mathbf{r}-\mathbf{r}'|} \sim \hat{\Omega}$  and further assuming a thin shell so neglecting differences in path length effects between different modes in the same relative geometry. Additionally, assuming a spherically symmetric source and shell geometry [where  $\rho$  can vary in  $\theta$  and  $\phi$  such that  $\rho R(\theta, \phi)$  is still 3D but  $R$  cannot] produces an analytic form for  $\tilde{P}$  that is circularly symmetric,

$$\tilde{P}_l^m \sim e^{-\frac{l}{2}\sigma^2}, \quad (3)$$

where  $\sigma$  characterizes the relative source size ( $L_{HS}$ ) to the shell size ( $L_{Shell}$ ) in radians (e.g.,  $\sigma \sim \text{atan}[L_{HS}/L_{Shell}]$ ) and is analogous to the point spread function of a point projection back-lighter.<sup>29</sup>

This provides an approximate expression to relate the  $\rho R$  to the measured yield asymmetry normalized by the average yield ( $\delta Y/Y_{avg}$ ). This implies that NAD activation measurements are most sensitive to low mode areal density asymmetries and yield anisotropies in response to  $\rho R$  asymmetries become increasingly small at higher mode. In practice, the assumptions used to obtain this simple expression will breakdown in realistic implosion hot-spot and shell geometries. Therefore, this expression should only be used to provide an order of magnitude estimate for how to relate these measurements as it could be off quantitatively by as much as a factor of  $\sim 2$ . Much more accurate approaches can be achieved numerically using Monte Carlo<sup>30</sup> or ray-tracing modeling and forward fit reconstructions.

## B. Understanding the relationship between $\rho R$ and down-scattered ratio (DSR)

Following a similar approach to the prior section but instead utilizing the second term of the Neumann series expansion allows us to express the 10–12 MeV flux ( $\varphi_{10-12}$ ) in terms of the source and scattering geometry as [see Fig. 1(b)]

$$\varphi_{10-12}(\mathbf{r}, \hat{\Omega}) = \int d^3 r' \frac{e^{-\Sigma_t |\mathbf{r}-\mathbf{r}'|}}{4\pi |\mathbf{r}-\mathbf{r}'|^2} \int d^3 r'' \times \int d\hat{\Omega}'' \Sigma_s(\hat{\Omega}'' \cdot \hat{\Omega}) \frac{e^{-\Sigma_t |\mathbf{r}'-\mathbf{r}''|}}{|\mathbf{r}'-\mathbf{r}''|^2} s(\mathbf{r}'', \hat{\Omega}''). \quad (4)$$

Here,  $\Sigma_s$  is the scattering macroscopic cross-section and  $\Sigma_{t*}$  is now the cross-section of the scattered neutron (as opposed to  $\Sigma_t$  for the 14 MeV source neutron). For simplicity we can neglect the attenuation of 10–12 MeV (“multi-scattering”) flux as the neutrons traverse the shell, which is a 10%–20% effect that is possible to include at the end. Written in this form, neglecting scattered neutron attenuation (or re-attenuation), and combined with the paraxial approximation,<sup>15</sup> the  $\delta DSR$  can be expressed as the normalized angular differential cross section ( $F_s$ ) convolved with  $\delta Y/Y_{avg}$

$$\delta DSR(\hat{\Omega}) \approx -\frac{0.046}{0.24} \int F_s(\hat{\Omega}'' \cdot \hat{\Omega}) * \delta Y(\hat{\Omega}'')/Y_{avg} d\hat{\Omega}'', \quad (5)$$

where the factors 0.24 and 0.046 are the per unit  $\rho R$  total probability of scattering and the probability of scattering into the 10–12 MeV bin, respectively (both in units of  $cm^2/g$ ). Physically, this is equivalent to redirecting a portion of the scattered neutrons into the appropriate kinematic trajectories for 14 MeV to 10–12 MeV scattering [see Fig. 1(c)]. And because the angular differential scattering cross section is already circularly symmetric, we can invoke the addition theorem to express this as

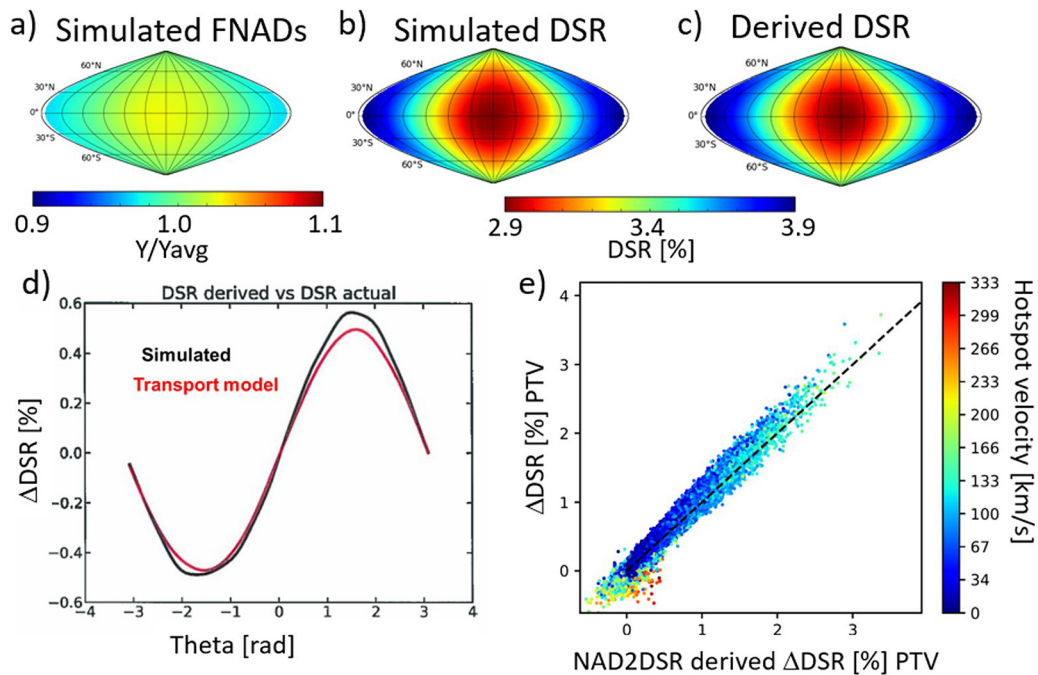
$$\delta\tilde{DSR}_l^m \approx -0.19 \sqrt{\frac{4\pi}{2l+1}} \tilde{F}_{sl}^m * \delta\tilde{Y}_l^m/Y_{avg}. \quad (6)$$

This expression was arrived at by assuming a shell-like geometry. However, unlike Eq. (3), Eq. (6) remains useful in more realistic non-spherical geometries because these more complex geometric effects are similar for both the NAD and DSRs. This will be evaluated with more realistic HYDRA simulations and geometries (with mode-1 and mode-2 asymmetries) in the following section.

This form provides a model that can quantitatively relate to the NADs and therefore  $\rho R$  to DSR. Perhaps more importantly, this relationship also reveals that the DSR and NADs are closely related by the angular differential cross section for 14 MeV neutrons scattering into the 10–12 MeV cone, effectively the blurring kernel of Fig. 1(c).

## C. Relationship between NADs and DSR

Equation (6) predicts a close relationship between NAD and DSR measurements of asymmetry in part because the source/shell blurring term appears in both the NAD and DSR measurements, similarly. We can test this prediction using detailed simulations using the radiation hydrodynamic code HYDRA.<sup>31</sup> Figures 2(a)–2(d) show the result of a 3D simulation with a single mode ( $\ell = 1, m = 1$ ) asymmetry in the radiation drive resulting in a asymmetric NAD and DSR



**FIG. 2.** (a)–(c) Simulated NAD, DSR, and inferred DSR distributions using Eq. (6) produced using single mode-1 3D HYDRA simulations. (d) Lineout comparisons of the DSR morphology as a function of azimuthal angle in radians. (e) Comparisons using 100k 2D ensemble simulations of P1 and P2 induced drive asymmetries. The results show that Eq. (6) predicts the DSR distribution well across the set.

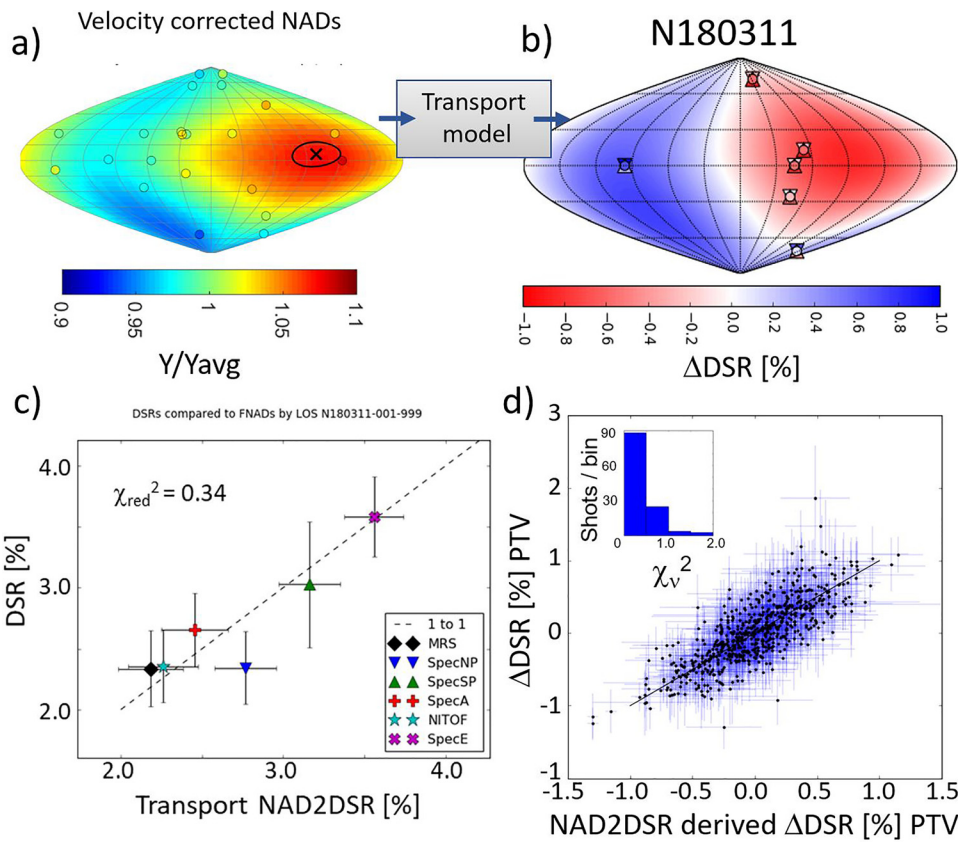
distribution. Also shown is the inferred DSR distribution as expected using this model. The results are in good agreement. Figure 2(e) shows a likewise comparison with 100 000 2D ensemble simulation with the simulated DSR vs the inferred DSR from the simulated NAD measurements. The model shows good agreement across the ensemble set showing that it is relatively robust even for complex geometries.

Having now established a method for comparing the NAD and DSR measurements, it is possible to compare the results of actual NIF experiments to test if the apparent asymmetries are consistent between the independent datasets. Figure 3(a) shows the measurement NAD distribution using the FNAD detector suite<sup>19,23</sup> from shot N180311. These data have been velocity corrected<sup>32,33</sup> to remove the impact of the Doppler shifted neutron energy on the activation data. Figure 3(b) shows the inferred DSR distribution of the  $Y_{lm}$  fit to the velocity corrected NAD data (background distribution) compared with the actual DSR measurements (points) from each available instrument (nTOFs and MRS)<sup>16,17</sup> with uncertainties indicated as up/down triangles underneath each point. The comparison shows that the two independent measurements are in good agreement. To show this more quantitatively, Fig. 3(c) plots the measured DSR from each individual instrument compared with the DSR inferred from the model using the NAD data. The reduced  $\chi^2$  between these two sets is 0.34. Figure 3(d) similarly plots the relative DSR from every instrument now for every available shot compared with the DSR inferred from the model using the NAD data. Inset on the plot is a histogram of the reduced  $\chi^2$  from each experiment showing excellent agreement across the dataset.

#### D. Inferring the solid angle average DSR ( $DSR_{4\pi}$ )

Equation (6) relates NAD and DSR measurements. However, it also helps reveal the underlying DSR morphology using the many NAD detectors ( $\sim 20$ – $50$ ) in contrast to the relatively few DSR measurements ( $\sim 5$ – $6$ ). In fact, the relative placement of those few DSR detectors can introduce a sampling bias when the underlying DSR distribution is asymmetric particularly because several detectors placed near each other will weigh that part of the solid angle more strongly than areas where the sampling is sparse. Additionally, the uncertainty weighted mean DSR ( $DSR_{uncw}$ ) is weighted by the instruments' relative uncertainties. This means that if, for example, a high DSR region in an asymmetric distribution is weighted more strongly because of both instrument placement and instrument uncertainties the  $DSR_{uncw}$  will be increased relative to the solid angle average DSR ( $DSR_{4\pi}$ ), or the opposite if low DSR region is weighted more heavily.

The DSR morphology inferred from Eq. (6) along with the measured NAD  $Y_{lm}$  distribution gives us a method to infer the shift of each line-of-sight that each measurement is made and remove the sampling bias to infer  $DSR_{4\pi}$ . The example shown in Fig. 3(c) shows a moderate level of asymmetry that happens to align a lower DSR region with a cluster of measurements around  $\sim 90$ – $315$  (NITOF, MRS, and SPECA). In this case, the uncertainty weighted  $DSR_{uncw}$  is  $2.7\% \pm 0.14\%$  while the  $DSR_{4\pi}$  is  $3.0\% \pm 0.16\%$  with an inferred shift  $DSR_{uncw} - DSR_{4\pi} = -0.26\% \pm 0.09\%$ . Figure 4 shows the result of repeating this analysis for all available experiments plotted as a histogram of the shift  $DSR_{uncw} - DSR_{4\pi}$ . The plot shows that shift is only significant for a fraction of shots but that it can be significant in some cases and may impact the interpretation of those experiments. It is

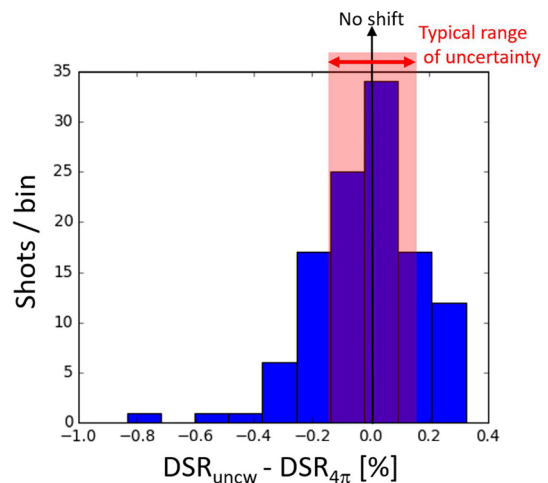


**FIG. 3.** (a) Velocity corrected NAD distribution<sup>32</sup> from shot N180311. (b) Inferred DSR distribution compared with actual DSR measurements (points) with uncertainties (upper and lower triangles underneath each point). The comparison shows that the magnitude and direction of the observed asymmetry agree between the inferred (background red and blue color scale) and the measured DSR (points) within measurement uncertainties. (c) DSR measurements from each instrument line-of-sight compared with the prediction. (d) DSR distribution for all experiments available compared to prediction. Inset is resultant chi-square distribution showing quantitative agreement across the measurement set.

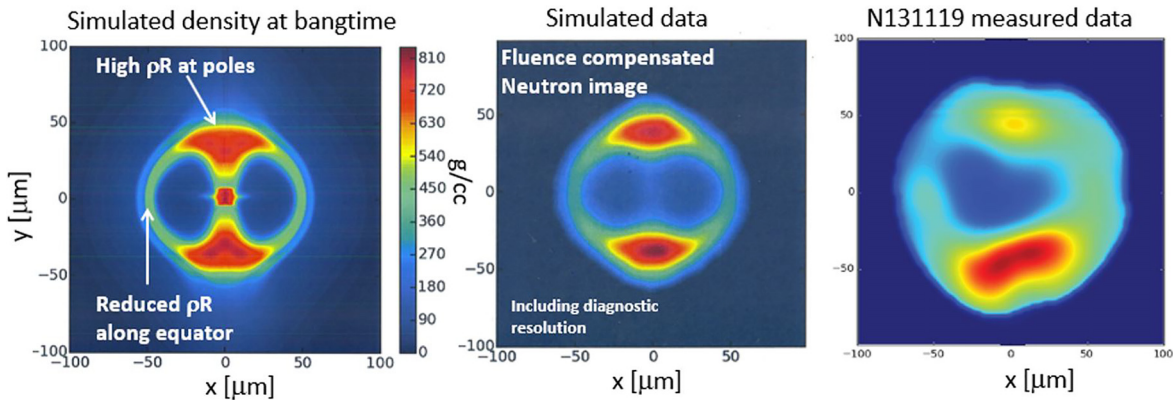
therefore important to recognize and compensate for this sampling bias, particularly in cases of large  $\ell = 1$  asymmetry. Several other techniques have been developed to infer the solid angle average DSR directly using a correlated  $Y_{lm}$  fit<sup>34</sup> to the multiple measurements of the DSR and using forward Monte Carlo transport modeling of the data.<sup>30</sup>

### III. MEASUREMENTS OF HIGHER MODE ASYMMETRY ( $\ell > 1$ )

To diagnose asymmetries beyond mode-1 ( $\ell > 1$ ), techniques such as Compton radiography,<sup>35</sup> neutron imaging,<sup>15,36,37</sup> and improved precision NAD activation measurements (RTNADs) have been developed. To help extract shell-symmetry information from down-scattered neutron images, two shell reconstruction techniques have recently been developed: a forward fit density reconstruction technique<sup>37</sup> and a primary fluence compensation technique.<sup>38</sup> The fluence compensation technique helps in part by removing the strong primary 14 MeV fluence effect in the down-scattered neutron image revealing the information most closely related to the imploded shell density (projected along the imaging line-of-sight (LOS) but limited by the neutron scattering kinematics). To better understand how this works in practice, 2D HYDRA postshot simulations of shot N131119



**FIG. 4.** Histogram of the difference between the uncertainty weighted average DSR ( $DSR_{uncw}$ ) and the inferred solid angle average DSR ( $DSR_{4\pi}$ ) for all available shots. The distribution shows that the shift is significant for only a relatively small fraction of shots, but also that in those shots it can be quite significant.

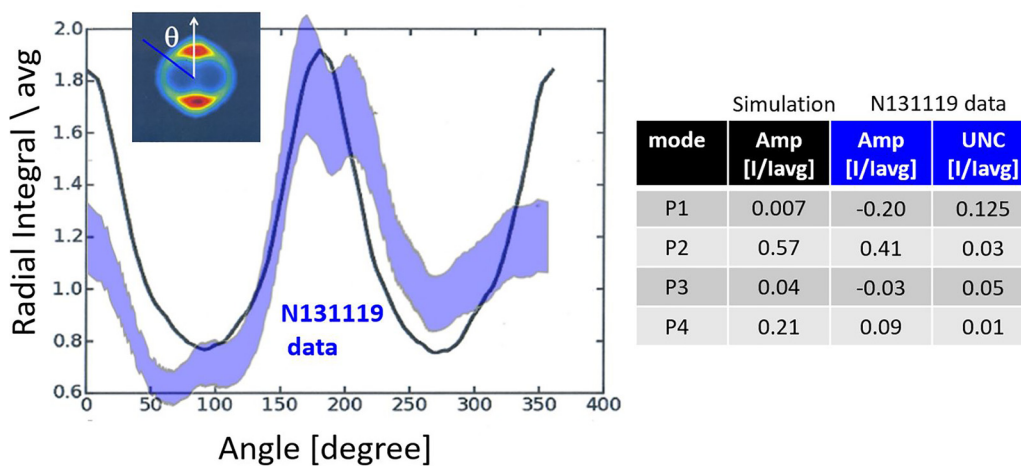


**FIG. 5.** (a) Postshot simulated density of N131119 including only radiation asymmetries induced by the laser/hohlraum at bangtime showing formation of a toroidal hotspot and “polar caps.” (b) Simulated fluence compensated image reconstructed from simulated diagnostic images including resolution showing much of the same character of the asymmetry in density. (c) Measured fluence compensated image from shot N131119 showing similar features to the measured data including the formation of polar caps. Notably, the measured data appear larger and less compressed with some evidence of P1 and higher mode 3D asymmetries.

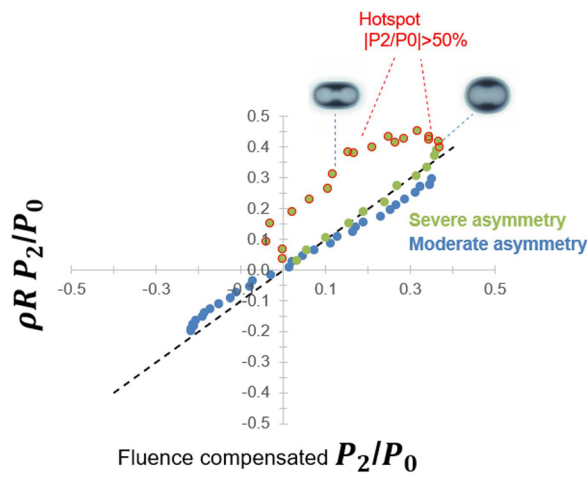
are shown in Fig. 5 that include only the radiation asymmetries induced by the delivered laser/hohlraum present in an axisymmetric 2D simulation. As is evident in the figure, this implosion had a significantly pole-hot drive leading to an accumulation of  $\rho R$  at the poles and an oblate hotspot that formed a torus after the collapse of two polar jets toward the center. The simulated density (a) can be compared to the simulated fluence compensated image (b) and both show the significant accumulation of  $\rho R$  at the poles. The images differ in where the jets reach the origin because of the reduced probability of neutrons to scatter off the central region into the 6–12 MeV down-scattered image and because of the reduced path length available for them to scatter along the thin column inside the torus. Figure 5(c) shows the measured fluence compensated image from N131119. Here much of the same character that was predicted by the simulation in Fig. 5(b) is observed in the experiment. Specifically, there are

significant polar features of increased  $\rho R$  and a toroidal hotspot as predicted. However, the fluence compensated image appears to be larger and thicker and shows evidence of higher mode 3D asymmetry.

To compare the observation with simulation more quantitatively, the fluence compensated image can be integrated in chords from the centroid of the primary neutron image outward and the integral plotted as a function of azimuthal angle. This quantity is somewhat analogous to  $\rho R$  (and will be compared to  $\rho R$  in the following paragraphs). A schematic of how this is done is shown in the inset of Fig. 6, along with the product of the integral itself plotted as a function of azimuthal angle (rotating counterclockwise) for the simulation (black curve) and the measurement (blue band) with an estimate of the measurement error. These curves can also be decomposed into Legendre polynomials, and the resulting coefficients compared, as is done on the table to the right of the plot. The measured data show less P2 and P4 when



**FIG. 6.** Quantitative comparison between measured and simulated images showing significant P2 asymmetry. The table shows the P1, P2, etc., amplitude of the Legendre decomposition of the simulated curves ( $I/l_{avg}$ ) in black and measured in blue (including estimated measurement uncertainty). Notably, the measured data show less P2 and P4 and also have some P1 not captured by the simulation.



**FIG. 7.** Comparison of the  $\rho R$  asymmetry vs the fluence compensated image asymmetry in term of the Legendre decomposed  $P_2/P_0$  for two sets of simulations with varying degrees of applied  $P_2$  asymmetry. The  $\rho R$  and fluence compensated  $P_2$  are fairly close until the shell becomes so distorted that the  $P_2$  no longer describes the dominant R asymmetry as power moves to higher modes.

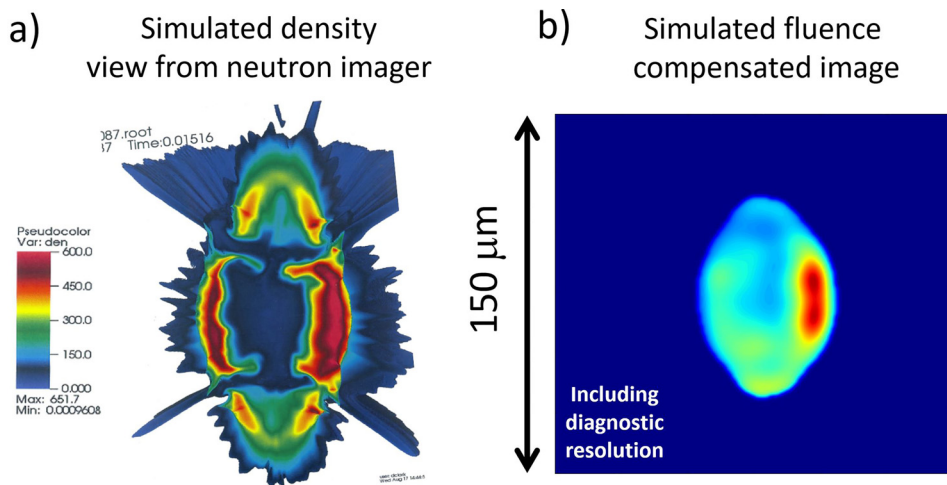
compared with the simulation but also show significant  $P_1$ . Note that the absolute alignment of the primary and down-scattered neutron images (co-registration) is particularly important in the mode-1 apparent in the fluence compensated image making the determination of  $P_1$  more challenging. However, Monte Carlo analysis can quantify this co-registration uncertainty for mode-1 and further shows it has negligible impact on the observation of higher mode asymmetries.

To help understand the relationship between  $\rho R$  and the fluence compensated image, two sets of 2D HYDRA simulations with varying degrees of  $P_2$  radiation asymmetry were performed. The results are shown in Fig. 7. The plot shows that fluence compensated  $P_2/P_0$  is closely related to the  $\rho R$   $P_2/P_0$  tracking to within  $\sim 20\%$  in these two datasets up until the point when the asymmetry becomes severe (hot-spot  $|P_2/P_0| > 50\%$ , or points with red circles). It should be noted that this relationship depends on the exact geometry of the hotspot and

shell. For example, as is noted in the prior figures, significant  $\rho R$  build up at the origin is more difficult to sample with the 6–12 MeV image. This is also apparent in Fig. 7 in the cases of severe asymmetry (points with red circles) when the Legendre  $P_2/P_0$  of both  $\rho R$  and the fluence compensated image saturate because of the generation of higher modes as the hotspot/shell becomes so distorted that  $P_2/P_0$  no longer captures the dominant asymmetry.

The effects of 3D asymmetries have been explored in high resolution simulations including hohlraum radiation asymmetries, capsule surface defects, the capsule support tent, and fill tube like that of N140819.<sup>39</sup> The simulated density at bangtime is shown in Fig. 8, cut in a plane perpendicular to the 90–315 imaging axis. Apparent is a prolate shell shape along with significant distortions due to the capsule and tent support perturbations. The simulated fluence compensated image is also shown. The prolate shell shape and hints of the tent perturbation are visible, but interestingly, a significant left/right asymmetry appears due to higher mode asymmetries that couple to the most sensitive part of the neutron scattering kinematics (about  $\sim 45^\circ$  from the imaging axis). This demonstrates that the fluence compensated image is sensitive to 3D asymmetries, even at relatively high mode. These results are consistent with findings of Crilly *et al.*<sup>22</sup> and McGlinchey *et al.*<sup>40</sup> However, importantly, a single line-of-sight is not enough information to fully reconstruct their morphology or character. Three lines-of-sight, particularly at roughly orthogonal angles, would provide a significantly more information of the implosion 3D asymmetry.<sup>37</sup> To that end, an additional gated neutron imaging line-of-sight has recently been commissioned and plans for a third are currently under development.

Measurements of  $\ell = 2$  can be validated in part by cross-comparing independent diagnostics, similar to the approach for  $\ell = 1$  shown in Sec. II. The presence of higher mode 3D asymmetries and the lack of enough lines-of-sight to fully constrain the picture make this more challenging. However, an attempt can be made with these challenges in mind by considering only  $P_2$  ( $\ell = 2, m = 0$ ) asymmetry projected along the hohlraum axis as measured by the RTNAD instrument suite and comparing that to the similarly defined  $P_2$  asymmetry from the fluence compensated image. This is shown in Fig. 9(a) where the RTNAD  $P_2$  is compared to the fluence compensated  $P_2$  with each



**FIG. 8.** (a) High-resolution postshot simulated density of N140819 in 3D including hohlraum radiation asymmetries, capsule surface defects, the capsule support tent, and fill tube.<sup>39</sup> (b) Simulated fluence compensated image for N140819 showing a prolate shell, hints of a tent perturbation, and a significant left/right asymmetry induced by higher mode 3D asymmetry.



point colored by the primary neutron image P2 in micrometer. Also shown are the simulation sets from Fig. 7 tracing out a 2d axisymmetric set of solutions for how these two measurements behave in these simulated examples. The result shows some consistency similar to that predicted by simulation, particularly in extreme P2 asymmetric cases. However, at smaller to moderate asymmetry, there is a significant amount of spread between these two measurements partly because of the transport issues described in Sec. II but also because of the presence of 3D asymmetries beyond P2. Figure 9(b) shows the RTNADs P2 as a function of the maximum contour P2 in micrometer from the fluence compensated image. Again, here the most extreme P2 asymmetries show a correspondence between the shell-shape and the RTNADs P2. The spread in points with more moderate P2 asymmetry may be the influence of higher mode and 3D asymmetries.

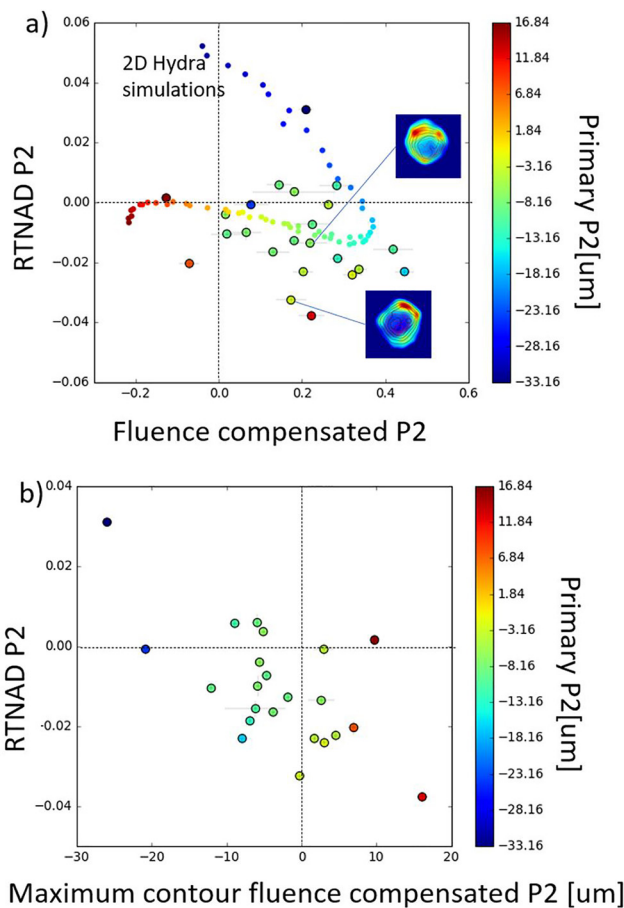


FIG. 9. (a) Measurements of P2 shell asymmetry from the RTNADs instrument suite compared to the fluence compensated image (larger points with black outlines). Also shown are 2d simulations including varying degrees of applied P2 radiation asymmetry (smaller points without outlines). The measurements often show significant P2 asymmetries but also show significant departures for 2D symmetry suggestive of 3D asymmetries. Two example shots are called out in the inset images showing what appears to be significant 3D structure. These two shots will be examined in more detail including an assessment of the 3D asymmetry in Figs. 11 and 12. (b) Comparison of the RTNADs P2 versus the P2 of the maximum contour of the fluence compensated image.

To understand if 3D asymmetries are indeed present and responsible for some of the spread in Fig. 9, the fluence compensated image can be raytraced using information about the source distribution from the primary neutron image to approximately account for the source size effects described in Sec. II to make a forward comparison with the NAD data along their common sampling regions. The kinematic scattering of 14 MeV neutrons into the 6–12 MeV down-scattered neutron image occurs at approximately  $\sim 45^\circ$  as indicated by the angular differential cross section. However, the finite-sized source sampling effect described by Sec. II broadens that distribution relative to the imaging line-of-sight to roughly  $\sim 70^\circ$ . Therefore, to compare the raytraced fluence compensated image to the RTNAD distribution, we have chosen a cone of  $70^\circ$  about the imaging line-of-sight. Figure 10(a) shows the simulated fluence compensated image from Fig. 5 with a schematic of the raytrace geometry used to compare the image to the RTNAD activation data. Figure 10(b) shows the results of that raytrace estimated NAD distribution (red curve) compared to actual simulated NAD distribution (black symbols) and NAD values with amplitudes corrected to correspond with a  $70^\circ$  cone about the equatorial neutron imaging axis (blue symbols). The results suggest that the approximate raytrace approach is sufficient to make a cleaner comparison between the two datasets. A more complete approach is currently under development with the forward density reconstruction of Volegov *et al.*<sup>37</sup>

Figure 11(a) shows the fluence compensated down-scattered neutron image data from 90–315 for shot N191007<sup>41,42</sup> along with a schematic of the raytracing (b). (c) shows the RTNAD activation data for shot N191007 (points) compared with a prediction for the  $Y/Y_{avg}$  from the raytraced fluence compensated image plotted in a cone 70 degrees from the 90–315 imaging line-of-sight (ring). (d) shows the prediction for the  $Y/Y_{avg}$  from the raytraced fluence compensated image plotted against (blue curve) the RTNAD data that lies within  $\sim 15^\circ$  of that cone, and the  $\ell = 2$   $Y_{lm}$  fit to the RTNAD data along the cone. The results show a generally consistent shell morphology suggesting significant shell asymmetry and structure. The underlying causes for this structure is an area of active area of research but may be caused by hydrodynamic instabilities coupling with drive<sup>43</sup> and high-density carbon (HDC) shell thickness seeded mode-1 asymmetries.<sup>44</sup>

As noted earlier, since the 6–12 MeV down-scattered neutron image is only sensitive to a portion (very roughly  $\sim 1/3$ ) of the solid angle of the shell  $\rho R$  facing toward the diagnostic line-of-sight,

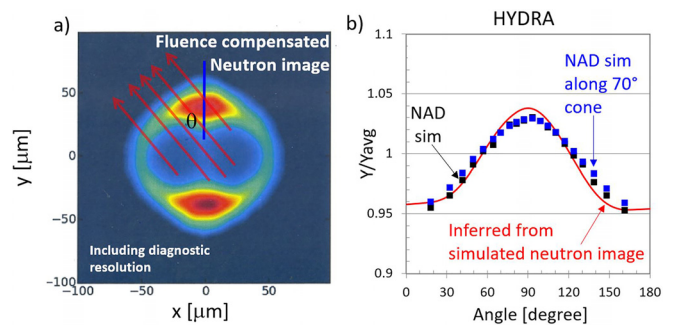
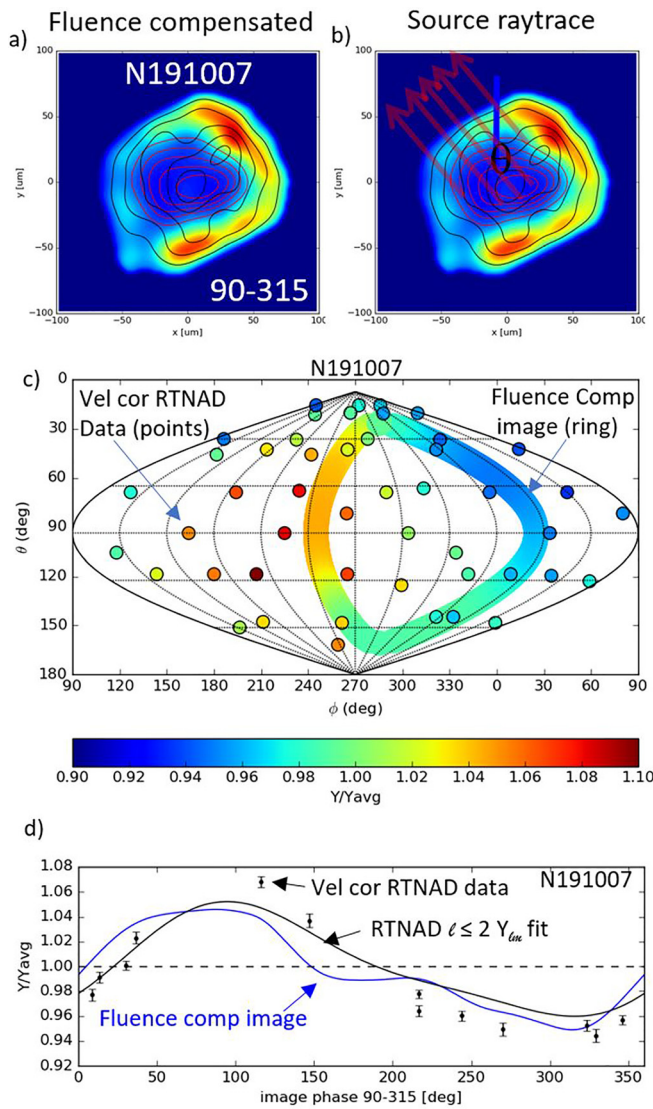


FIG. 10. (a) Simulated fluence compensated image with schematic of raytrace geometry. (b) Simulated NAD distribution compared with inferred NAD distribution from raytraced simulated fluence compensated image. The comparison shows this is a useful way to compare the two independent measurements.

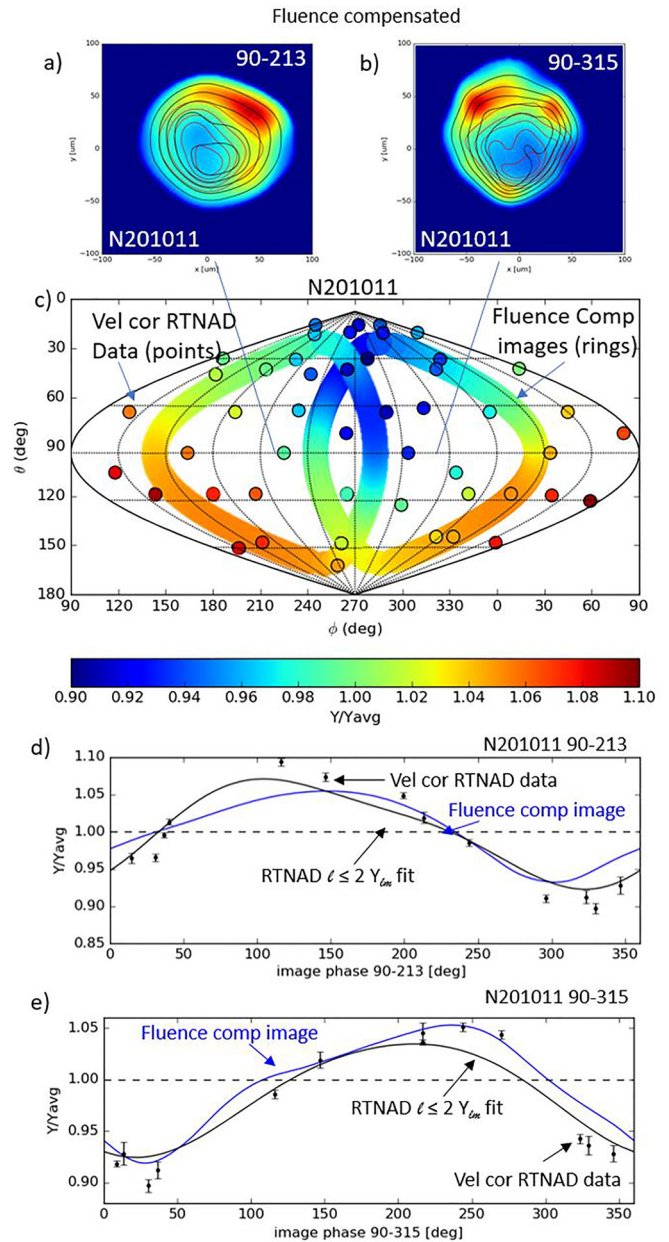
multiple lines-of-sight are required to fully sample and reconstruct the full  $4\pi$  shell morphology.<sup>37</sup> To that end, an additional down-scattered line-of-sight has recently been installed and commissioned on the 90–213 axis which provides another independent view of the primary and down-scattered neutron images. From this view, the fluence compensated image can then be compared to that of the 90–315 axis. Figure 12 shows the preliminary 90–213 data from shot N201011<sup>41</sup> compared with the 90–315 data from the same experiment. Both images show a significant amount of  $\ell = 1$  3D asymmetry and higher mode structure. To compare these two images and contrast against the independent RTNAD instrument suite, both LOSs were raytraced and



**FIG. 11.** (a) Fluence compensated image for shot N191007 showing a significant structure. (b) Schematic of raytracing to numerically account for source-size effects described in Sec. II. (c) Raytraced fluence compensated image projected onto velocity corrected RTNAD data sky at  $70^\circ$  from 90–315. (d) Velocity corrected RTNAD activation data (within  $\sim 15^\circ$  of the cone trajectory) for shot N191007 compared to the raytraced fluence.

plotted against the RTNAD data in Fig. 12(c). The results are generally consistent, suggesting that significant 3D  $\rho R$  is present in this experiment.

As more data are collected with both 90–213 and 90–315 NIS primary and neutron images, that data will be trended against the



**FIG. 12.** (a) Preliminary fluence compensated image from the newly installed and commissioned 90–213 line-of-sight for shot N201011. (b) Fluence compensated image from the 90–315 line-of-sight. (c) Velocity corrected RTNAD data compared to raytraced fluence compensated images from the two lines-of-sight. The two neutron imaging lines-of-sight and velocity corrected RTNAD data are generally consistent, suggesting 3D asymmetry and significant shell structure.

RTNAD data to see if the observed  $\ell > 1$  mode structures are consistent for a larger set of experiments. Additionally, the forward density reconstruction technique lends itself to including multiple lines-of-sight and is being employed to develop an improved understanding of the 3D  $\rho R$ .<sup>37</sup> Eventually, a line-of-sight installed near the north pole would likely add significantly to the understanding of  $\ell > 1$  3D asymmetries in experiments at the NIF.

#### IV. SUMMARY

In summary, three-dimensional low-mode areal density asymmetries are present and significant in NIF implosions. Low-mode asymmetries damage implosion performance by reducing the available energy to convert to internal hotspot energy and degrading the confinement of that energy. Mode-1 asymmetries as diagnosed through the neutron hotspot velocity, the NAD activation suites (RTNAD and FNAD), and the down-scattered ratios have been used to corroborate and correlate these asymmetries. The principal sources of mode-1 observations are now being traced to their origins.<sup>43</sup>

Diagnosing asymmetries beyond mode-1 is significantly more challenging. However, Compton radiography,<sup>35</sup> neutron imaging, and improved precision on the NAD activation suite (RTNAD) are opening up avenues to attempt to reconstruct higher mode implosion asymmetries. An analysis of the fluence compensated<sup>38</sup> down-scattered neutron image compared with simulation and compared with the RTNAD suite shows evidence of Legendre mode P2 asymmetry as well as higher order 3D asymmetries. Comparisons with simulation show that the imploded dense DT shell is significantly thicker and larger than predicted, consistent with the observation of lower DSR, suggesting less compression. This result is consistent with the observations of Tommasini *et al.* with Compton radiography,<sup>35</sup> building confidence that simulations currently overpredict the compressibility of the dense DT fuel. This may be a result of higher mode instabilities (beyond what is resolvable) generating entropy and making the dense DT less compressible.

The data also indicate significant 3D asymmetries. These 3D asymmetries are challenging to diagnose with a single neutron imager line-of-sight. Nevertheless, forward comparisons with the RTNAD activation suite are favorable, lending confidence that the inferred asymmetries are real, at least in low mode. To better diagnose these 3D objects, a second neutron imager line of sight has recently been commissioned and early data add significantly to the apparent 3D asymmetries observed and providing further validation. Plans for a third neutron imaging line-of-sight are under development as are plans for two-axis Compton radiography. This will significantly improve reconstructions of the 3D  $\rho R$  distribution and the ability to estimate the impact and causes of these asymmetries.

#### ACKNOWLEDGMENTS

The authors sincerely thank the NIF operations staff who supported this work. Raw data were generated at the NIF. This work was performed under the auspices of the U.S. Department of Energy by Lawrence Livermore National Laboratory under Contract No. DE-AC52-07NA27344.

#### DATA AVAILABILITY

The data that support the findings of this study are available from the corresponding author upon reasonable request.

#### REFERENCES

- <sup>1</sup>E. I. Moses, *J. Phys.* **112**(1), 012003 (2008).
- <sup>2</sup>J. D. Lindl, P. Amendt, R. L. Berger, S. G. Glendinning, S. H. Glenzer, S. W. Haan, R. L. Kauffman, O. L. Landen, and L. J. Suter, *Phys. Plasmas* **11**, 339 (2004).
- <sup>3</sup>S. Atzeni and J. Meyer-ter-Vehn, *The Physics of Inertial Fusion* (Oxford University Press, Oxford, 2004).
- <sup>4</sup>J. P. Freidberg, *Plasma Physics and Fusion Energy* (Cambridge University Press, Cambridge, 2007).
- <sup>5</sup>R. Betti, P. Y. Chang, B. K. Spears, K. S. Anderson, J. Edwards, M. Fatenejad, J. D. Lindl, R. L. McCrory, R. Nora, and D. Shvarts, *Phys. Plasmas* **17**(5), 058102 (2010).
- <sup>6</sup>O. A. Hurricane, P. T. Springer, P. K. Patel, D. A. Callahan, K. Baker, D. T. Casey, L. Divol, T. Döppner, D. E. Hinkel, M. Hohenberger, L. F. Berzak Hopkins, C. Jarrott, A. Kritcher, S. L. Pape, S. Maclaren, L. Masse, A. Pak, J. Ralph, C. Thomas, P. Volegov, and A. Zylstra, *Phys. Plasmas* **26**(5), 052704 (2019).
- <sup>7</sup>O. A. Hurricane, D. T. Casey, O. Landen, A. L. Kritcher, R. Nora, P. K. Patel, J. A. Gaffney, K. D. Humbird, J. E. Field, M. K. G. Kruse, J. L. Peterson, and B. K. Spears, *Phys. Plasmas* **27**(6), 062704 (2020).
- <sup>8</sup>M. J. Schlossberg, D. T. Casey, J. A. Frenje, C.-K. Li, F. H. Seguin, R. D. Petrasso, R. Ashabranner, R. Bionta, S. LePape, M. McKernan, A. Mackinnon, J. D. Kilkenny, J. Knauer, and T. C. Sangster, *Phys. Plasmas* **20**(4), 042707 (2013).
- <sup>9</sup>D. Eder, B. Spears, D. Casey, A. Pak, T. Ma, N. Izumi, B. Pollock, C. Weber, A. Kritcher, O. Jones, J. Milovich, R. Town, H. Robey, D. Hinkel, D. Callahan, S. Hatchett, J. Knauer, C. Yeaman, D. Bleuel, S. Nagel, R. Hatarik, S. Khan, D. Sayre, J. Caggiano, G. Grim, M. Eckart, D. Fittinghoff, F. Merrill, and D. Bradley, *J. Phys.* **717**(1), 012014 (2016).
- <sup>10</sup>D. J. Schlossberg, G. P. Grim, D. T. Casey, A. S. Moore, R. Nora, B. Bachmann, L. R. Benedetti, R. M. Bionta, M. J. Eckart, J. E. Field, D. N. Fittinghoff, M. Gatu Johnson, V. Geppert-Kleinrath, E. P. Hartouni, R. Hatarik, W. W. Hsing, L. C. Jarrott, S. F. Khan, J. D. Kilkenny, O. L. Landen, B. J. MacGowan, A. J. Mackinnon, K. D. Meaney, D. H. Munro, S. R. Nagel, A. Pak, P. K. Patel, B. K. Spears, P. L. Volegov, and C. V. Young, Observation of hydrodynamic flows within imploding fusion plasmas on the National Ignition Facility. *Phys. Rev. Lett.* (submitted).
- <sup>11</sup>A. L. Kritcher, R. Town, D. Bradley, D. Clark, B. Spears, O. Jones, S. Haan, P. T. Springer, J. Lindl, R. H. H. Scott, D. Callahan, M. J. Edwards, and O. L. Landen, *Phys. Plasmas* **21**(4), 042708 (2014).
- <sup>12</sup>O. A. Hurricane, private communication (August 2020).
- <sup>13</sup>F. E. Merrill, D. Bower, R. Buckles, D. D. Clark, C. R. Danly, O. B. Drury, J. M. Dzenitis, V. E. Fatherley, D. N. Fittinghoff, R. Gallegos, G. P. Grim, N. Guler, E. N. Loomis, S. Lutz, R. M. Malone, D. D. Martinson, D. Mares, D. J. Morley, G. L. Morgan, J. A. Oertel, I. L. Tregillis, P. L. Volegov, P. B. Weiss, C. H. Wilde, and D. C. Wilson, *Rev. Sci. Instrum.* **83**(10), 10D317 (2012).
- <sup>14</sup>G. P. Grim, N. Guler, F. E. Merrill, G. L. Morgan, C. R. Danly, P. L. Volegov, C. H. Wilde, D. C. Wilson, D. S. Clark, D. E. Hinkel, O. S. Jones, K. S. Raman, N. Izumi, D. N. Fittinghoff, O. B. Drury, E. T. Alger, P. A. Arnold, R. C. Ashabranner, L. J. Atherton, M. A. Barrios, S. Batha, P. M. Bell, L. R. Benedetti, R. L. Berger, L. A. Bernstein, L. V. Berzins, R. Betti, S. D. Bhandarkar, R. M. Bionta, D. L. Bleuel, T. R. Boehly, E. J. Bond, M. W. Bowers, D. K. Bradley, G. K. Brunton, R. A. Buckles, S. C. Burkhart, R. F. Burr, J. A. Caggiano, D. A. Callahan, D. T. Casey, C. Castro, P. M. Celliers, C. J. Cerjan, G. A. Chandler, C. Choate, S. J. Cohen, G. W. Collins, G. W. Cooper, J. R. Cox, J. R. Cradick, P. S. Datte, E. L. Dewald, P. D. Nicola, J. M. D. Nicola, L. Divol, S. N. Dixit, R. Dylla-Spears, E. G. Dzenitis, M. J. Eckart, D. C. Eder, D. H. Edgell, M. J. Edwards, J. H. Eggert, R. B. Ehrlich, G. V. Erbert, J. Fair, D. R. Farley, B. Felker, R. J. Fortner, J. A. Frenje, G. Frieders, S. Friedrich, M. Gatu-Johnson, C. R. Gibson, E. Giraldez, V. Y. Glebov, S. M. Glenn, S. H. Glenzer, G. Gururangan, S. W. Haan, K. D. Hahn, B. A. Hammel, A. V. Hamza, E. P. Hartouni, R. Hatarik, S. P. Hatchett, C. Haynam, M. R. Hermann, H. W. Herrmann, D. G. Hicks, J. P. Holder, D. M. Holunga, J. B. Horner, W. W. Hsing, H. Huang, M. C. Jackson, K. S. Jancaitis, D. H. Kalantar, R. L. Kauffman, M. I. Kauffman, S. F. Khan, J. D. Kilkenny, J. R. Kimbrough, R. Kirkwood, J. L. Kline, J. P. Knauer, K. M. Knittel, J. A. Koch, T. R. Kohut, B. J. Koziolowski, K. Krauter, G. W. Krauter, A. L. Kritcher, J. Kroll, G. A. Kyrala, K. N. L. Fortune, G. LaCaille, L. J. Lagin, T. A. Land, O. L. Landen, D. W. Larson, D. A. Latray, R. J. Leeper, T. L. Lewis, S. LePape, J. D. Lindl, R. R. Lowe-Webb, T. Ma, B. J. MacGowan, A. J. MacKinnon, A. G. MacPhee, R. M. Malone, T. N. Malsbury, E. Mapoles, C. D. Marshall, D. G. Mathisen, P. McKenty, J. M. McNaney, N. B. Meezan, P.

- Michel, J. L. Milovich, J. D. Moody, A. S. Moore, M. J. Moran, K. Moreno, E. I. Moses, D. H. Munro, B. R. Nathan, A. J. Nelson, A. Nikroo, R. E. Olson, C. Orth, A. E. Pak, E. S. Palma, T. G. Parham, P. K. Patel, R. W. Patterson, R. D. Petrasso, R. Prasad, J. E. Ralph, S. P. Regan, H. Rinderknecht, H. F. Robey, G. F. Ross, C. L. Ruiz, F. H. Seguin, J. D. Salmonson, T. C. Sangster, J. D. Sater, R. L. Saunders, M. B. Schneider, D. H. Schneider, M. J. Shaw, N. Simanovskaia, B. K. Spears, P. T. Springer, C. Stoeckl, W. Stoeffl, L. J. Suter, C. A. Thomas, R. Tommasini, R. P. Town, A. J. Traille, B. V. Wontergem, R. J. Wallace, S. Weaver, S. V. Weber, P. J. Wegner, P. K. Whitman, K. Widmayer, C. C. Widmayer, R. D. Wood, B. K. Young, R. A. Zacharias, and A. Zylstra, *Phys. Plasmas* **20**(5), 056320 (2013).
- <sup>15</sup>P. Volegov, C. R. Danly, D. N. Fittinghoff, G. P. Grim, N. Guler, N. Izumi, T. Ma, F. E. Merrill, A. L. Warrick, C. H. Wilde, and D. C. Wilson, *Rev. Sci. Instrum.* **85**(2), 023508 (2014).
- <sup>16</sup>R. Hatarik, D. B. Sayre, J. A. Caggiano, T. Phillips, M. J. Eckart, E. J. Bond, C. Cerjan, G. P. Grim, E. P. Hartouni, J. P. Knauer, J. M. McNaney, and D. H. Munro, *J. Appl. Phys.* **118**(18), 184502 (2015).
- <sup>17</sup>M. G. Johnson, J. A. Frenje, D. T. Casey, C. K. Li, F. H. Seguin, R. Petrasso, R. Ashabranner, R. M. Bionta, D. L. Bleuel, E. J. Bond, J. A. Caggiano, A. Carpenter, C. J. Cerjan, T. J. Clancy, T. Doepfner, M. J. Eckart, M. J. Edwards, S. Friedrich, S. H. Glenzer, S. W. Haan, E. P. Hartouni, R. Hatarik, S. P. Hatchett, O. S. Jones, G. Kyrala, S. L. Pape, R. A. Lerche, O. L. Landen, T. Ma, A. J. MacKinnon, M. A. McKernan, M. J. Moran, E. Moses, D. H. Munro, J. McNaney, H. S. Park, J. Ralph, B. Remington, J. R. Rygg, S. M. Sepke, V. Smalyuk, B. Spears, P. T. Springer, C. B. Yeamans, M. Farrell, D. Jason, J. D. Kilkenny, A. Nikroo, R. P. Paguio, J. P. Knauer, V. Y. Glebov, T. C. Sangster, R. Betti, C. Stoeckl, J. Magoon, M. J. Shoup III, G. P. Grim, J. Kline, G. L. Morgan, T. J. Murphy, R. J. Leeper, C. L. Ruiz, G. W. Cooper, and A. J. Nelson, *Rev. Sci. Instrum.* **83**(10), 10D308 (2012).
- <sup>18</sup>J. A. Frenje, R. Bionta, E. J. Bond, J. A. Caggiano, D. T. Casey, C. Cerjan, J. Edwards, M. Eckart, D. N. Fittinghoff, S. Friedrich, V. Y. Glebov, S. Glenzer, G. Grim, S. Haan, R. Hatarik, S. Hatchett, M. G. Johnson, O. S. Jones, J. D. Kilkenny, J. P. Knauer, O. Landen, R. Leeper, S. L. Pape, R. Lerche, C. K. Li, A. MacKinnon, J. McNaney, F. E. Merrill, M. Moran, D. H. Munro, T. J. Murphy, R. D. Petrasso, R. Rygg, T. C. Sangster, F. H. Seguin, S. Sepke, B. Spears, P. Springer, C. Stoeckl, and D. C. Wilson, *Nucl. Fusion* **53**(4), 043014 (2013).
- <sup>19</sup>C. B. Yeamans and D. L. Bleuel, *Fusion Sci. Technol.* **72**(2), 120–128 (2017).
- <sup>20</sup>F. B. Brown, R. F. Barrett, T. E. Booth, J. S. Bull, L. J. Cox, R. A. Forster, T. J. Goorley, R. D. Mosteller, S. E. Post, R. E. Prael, E. C. Selcow, A. Sood, and J. Sweezy, *Trans. Am. Nucl. Soc.* **87**, 273 (2002).
- <sup>21</sup>J. P. Chittenden, B. D. Appelbe, F. Manke, K. McGlinchey, and N. P. L. Niasse, *Phys. Plasmas* **23**(5), 052708 (2016).
- <sup>22</sup>A. J. Crilly, B. D. Appelbe, C. McGlinchey, C. A. Walsh, J. K. Tong, A. B. Boxall, and J. P. Chittenden, *Phys. Plasmas* **25**(12), 122703 (2018).
- <sup>23</sup>D. L. Bleuel, C. B. Yeamans, L. A. Bernstein, R. M. Bionta, J. A. Caggiano, D. T. Casey, G. W. Cooper, O. B. Drury, J. A. Frenje, C. A. Hagmann, R. Hatarik, J. P. Knauer, M. G. Johnson, K. M. Knittel, R. J. Leeper, J. M. McNaney, M. Moran, C. L. Ruiz, and D. H. G. Schneider, *Rev. Sci. Instrum.* **83**(10), 10D313 (2012).
- <sup>24</sup>R. M. Bionta, G. P. Grim, K. D. Hahn, E. P. Hartouni, E. A. Henry, H. Y. Khater, A. S. Moore, and D. J. Schlossberg, “Real-time nuclear activation detectors for measuring neutron angular distributions at the National Ignition Facility,” *Rev. Sci. Instrum.* (to be published).
- <sup>25</sup>J. J. Duderstadt and W. R. Martin, *Transport Theory* (Wiley, Chichester, UK, 1979).
- <sup>26</sup>Note in this manuscript we will use both 3D spherical harmonic decompositions (Y<sub>lm</sub>) and 2D symmetric Legendre decompositions (P<sub>1</sub>, P<sub>2</sub>, etc.), explicitly describing which decomposition is being used as they are related but not the same.
- <sup>27</sup>R. Basri and D. W. Jacobs, *IEEE Trans. Pattern Anal. Mach. Intell.* **25**(2), 218–233 (2003).
- <sup>28</sup>D. T. Casey, J. A. Frenje, M. G. Johnson, F. H. Seguin, C. K. Li, R. D. Petrasso, V. Y. Glebov, J. Katz, J. P. Knauer, D. D. Meyerhofer, T. C. Sangster, R. M. Bionta, D. L. Bleuel, T. Doepfner, S. Glenzer, E. Hartouni, S. P. Hatchett, S. L. Pape, T. Ma, A. MacKinnon, M. A. McKernan, M. Moran, E. Moses, H.-S. Park, J. Ralph, B. A. Remington, V. Smalyuk, C. B. Yeamans, J. Kline, G. Kyrala, G. A. Chandler, R. J. Leeper, C. L. Ruiz, G. W. Cooper, A. J. Nelson, K. Fletcher, J. Kilkenny, M. Farrell, D. Jason, and R. P. Paguio, *Rev. Sci. Instrum.* **83**(10), 10D912 (2012).
- <sup>29</sup>H.-S. Park, B. R. Maddox, E. Giraldez, S. P. Hatchett, L. T. Hudson, N. Izumi, M. H. Key, S. L. Pape, A. J. MacKinnon, A. G. MacPhee, P. K. Patel, T. W. Phillips, B. A. Remington, J. F. Seely, R. Tommasini, R. Town, J. Workman, and E. Brambrink, *Phys. Plasmas* **15**(7), 072705 (2008).
- <sup>30</sup>R. M. Bionta, “Fuel areal density distributions derived from nuclear scattering signatures” (unpublished).
- <sup>31</sup>M. M. Marinak, G. D. Kerbel, N. A. Gentile, O. Jones, D. Munro, S. Pollaine, T. R. Dittrich, and S. W. Haan, *Phys. Plasmas* **8**(5), 2275–2280 (2001).
- <sup>32</sup>H. G. Rinderknecht, R. Bionta, G. Grim, R. Hatarik, H. Khater, D. Schlossberg, and C. Yeamans, *Rev. Sci. Instrum.* **89**(10), 10I125 (2018).
- <sup>33</sup>H. G. Rinderknecht, D. T. Casey, R. Hatarik, R. M. Bionta, B. J. MacGowan, P. Patel, O. L. Landen, E. P. Hartouni, and O. A. Hurricane, *Phys. Rev. Lett.* **124**(14), 145002 (2020).
- <sup>34</sup>E. P. Hartouni, R. M. Bionta, D. T. Casey, M. J. Eckart, M. Gatu-Johnson, G. P. Grim, K. D. Hahn, J. Jeet, S. M. Kerr, A. L. Kritcher, B. J. MacGowan, A. S. Moore, D. H. Munro, D. J. Schlossberg, and A. Zylstra, *Rev. Sci. Instrum.* **92**, 043512 (2021).
- <sup>35</sup>R. Tommasini, O. L. Landen, L. Berzak Hopkins, S. P. Hatchett, D. H. Kalantar, W. W. Hsing, D. A. Alessi, S. L. Ayers, S. D. Bhandarkar, M. W. Bowers, D. K. Bradley, A. D. Conder, J. M. Di Nicola, P. D. Nicola, L. Divol, D. Fittinghoff, G. Gururangan, G. N. Hall, M. Hamamoto, D. R. Hargrove, E. P. Hartouni, J. E. Heebner, S. I. Herriot, M. R. Hermann, J. P. Holder, D. M. Holunga, D. Homoelle, C. A. Iglesias, N. Izumi, A. J. Kemp, T. Kohut, J. J. Kroll, K. LaFortune, J. K. Lawson, R. Lowe-Webb, A. J. MacKinnon, D. Martinez, N. D. Masters, M. P. Mauldin, J. Milovich, A. Nikroo, J. K. Okui, J. Park, M. Prantl, L. J. Pelz, M. Schoff, R. Sigurdsson, P. L. Volegov, S. Vohof, T. L. Zobrist, R. J. Wallace, C. F. Walters, P. Wegner, C. Widmayer, W. H. Williams, K. Youngblood, M. J. Edwards, and M. C. Herrmann, *Phys. Rev. Lett.* **125**(15), 155003 (2020).
- <sup>36</sup>P. L. Volegov, D. C. Wilson, E. L. Dewald, L. F. Berzak Hopkins, C. R. Danly, V. E. Fatherley, V. Geppert-Kleinrath, F. E. Merrill, R. Simpson, C. H. Wilde, D. N. Fittinghoff, D. T. Casey, G. P. Grim, M. J. Ayers, R. Hatarik, C. B. Yeamans, M. K. G. Kruse, D. B. Sayre, D. Munro, S. L. Pape, N. Izumi, and S. H. Batha, *Phys. Plasmas* **25**(6), 062708 (2018).
- <sup>37</sup>P. L. Volegov, S. H. Batha, V. Geppert-Kleinrath, C. R. Danly, F. E. Merrill, C. H. Wilde, D. C. Wilson, D. T. Casey, D. Fittinghoff, B. Appelbe, J. P. Chittenden, A. J. Crilly, and K. McGlinchey, *J. Appl. Phys.* **127**(8), 083301 (2020).
- <sup>38</sup>D. T. Casey, P. L. Volegov, F. E. Merrill, D. H. Munro, G. P. Grim, O. L. Landen, B. K. Spears, D. N. Fittinghoff, J. E. Field, and V. A. Smalyuk, *Rev. Sci. Instrum.* **87**(11), 11E715 (2016).
- <sup>39</sup>D. S. Clark, C. R. Weber, J. L. Milovich, J. D. Salmonson, A. L. Kritcher, S. W. Haan, B. A. Hammel, D. E. Hinkel, O. A. Hurricane, O. S. Jones, M. M. Marinak, P. K. Patel, H. F. Robey, S. M. Sepke, and M. J. Edwards, *Phys. Plasmas* **23**(5), 056302 (2016).
- <sup>40</sup>K. McGlinchey, B. D. Appelbe, A. J. Crilly, J. K. Tong, C. A. Walsh, and J. P. Chittenden, *Phys. Plasmas* **25**(12), 122705 (2018).
- <sup>41</sup>A. B. Zylstra, A. L. Kritcher, O. A. Hurricane, D. A. Callahan, K. Baker, T. Braun, D. T. Casey, D. Clark, K. Clark, T. Doepfner, L. Divol, D. E. Hinkel, M. Hohenberger, C. Kong, O. L. Landen, A. Nikroo, A. Pak, P. Patel, J. E. Ralph, N. Rice, R. Tommasini, M. Schoff, M. Stadermann, D. Strozzi, C. Weber, C. Young, C. Wild, R. P. J. Town, and M. J. Edwards, *Phys. Rev. Lett.* **126**(2), 025001 (2021).
- <sup>42</sup>A. L. Kritcher, D. T. Casey, C. A. Thomas, A. B. Zylstra, M. Hohenberger, K. Baker, S. Le Pape, B. Bachmann, S. Bhandarkar, J. Biener, T. Braun, D. Clark, L. Divol, T. Doepfner, D. Hinkel, C. Kong, D. Mariscal, M. Millot, J. Milovich, A. Nikroo, A. Pak, N. Rice, H. Robey, M. Stadermann, J. Sevier, D. Strozzi, C. Weber, C. Wild, B. Woodworth, J. Edwards, D. A. Callahan, and O. A. Hurricane, *Phys. Plasmas* **27**(5), 052710 (2020).
- <sup>43</sup>B. J. MacGowan, O. L. Landen, D. T. Casey, C. V. Young, D. A. Callahan, E. P. Hartouni, R. Hatarik, M. Hohenberger, T. Ma, D. Mariscal, A. Moore, R. Nora, H. Rinderknecht, D. Schlossberg, and B. M. Van Wontergem, *Trending Low Mode Asymmetries in NIF Capsule Drive using a Simple Viewfactor Metric*. High Energy Density Phys. (submitted).
- <sup>44</sup>D. T. Casey, B. J. MacGowan, J. D. Sater, A. B. Zylstra, O. L. Landen, J. Milovich, O. A. Hurricane, A. L. Kritcher, M. Hohenberger, K. Baker, S. Le Pape, T. Doepfner, C. Weber, H. Huang, C. Kong, J. Biener, C. V. Young, S. Haan, R. C. Nora, S. Ross, H. Robey, M. Stadermann, A. Nikroo, D. A. Callahan, R. M. Bionta, K. D. Hahn, A. S. Moore, D. Schlossberg, M. Bruhn, K. Sequoia, N. Rice, M. Farrell, and C. Wild, *Phys. Rev. Lett.* **126**(2), 025002 (2021).